Diagnostic power of diffuse reflectance spectroscopy for targeted detection of breast lesions with microcalcifications

Jaqueline S. Soares[a,1], Ishan Barman[a,1], Narahara Chari Dingari[a,1], Zoya Volynskaya[a,2], Wendy Liu[b,c], Nina Klein[b,c], Donna Plecha[b,c], Ramachandra R. Dasari[a], and Maryann Fitzmaurice[b,3]

[a]George R. Harrison Spectroscopy Laboratory, Massachusetts Institute of Technology, Cambridge, MA 02139; [b]Departments of Pathology and Radiology, Case Western Reserve University, Cleveland, OH 44106; and [c]Departments of Pathology and Radiology, University Hospitals Case Medical Center, Cleveland, OH 44106

Microcalcifications geographically target the location of abnormalities within the breast and are of critical importance in breast cancer diagnosis. However, despite stereotactic guidance, core needle biopsy fails to retrieve microcalcifications in up to 15% of patients. Here, we introduce an approach based on diffuse reflectance spectroscopy for detection of microcalcifications that focuses on variations in optical absorption stemming from the calcified clusters and the associated cross-linking molecules. In this study, diffuse reflectance spectra are acquired ex vivo from 203 sites in fresh biopsy tissue cores from 23 patients undergoing stereotactic breast needle biopsies. By correlating the spectra with the corresponding radiographic and histologic assessment, we have developed a support vector machine-derived decision algorithm, which shows high diagnostic power (positive predictive value and negative predictive value of 97% and 88%, respectively) for diagnosis of lesions with microcalcifications. We further show that these results are robust and not due to any spurious correlations. We attribute our findings to the presence of proteins (such as elastin), and desmosine and isodesmosine cross-linkers in the microcalcifications. It is important to note that the performance of the diffuse reflectance decision algorithm is comparable to one derived from the corresponding Raman spectra, and the considerably higher intensity of the reflectance signal enables the detection of the targeted lesions in a fraction of the spectral acquisition time. Our findings create a unique landscape for spectroscopic validation of breast core needle biopsy for detection of microcalcifications that can substantially improve the likelihood of an adequate, diagnostic biopsy in the first attempt.

histopathology | mammography | real-time guidance

According to the latest American Cancer Society statistics, an estimated 226,870 and 63,300 new cases of invasive and in situ breast cancer, respectively, are expected to occur among women in the United States in 2012 (1). The general consensus in the clinical community is that the morbidity and mortality of breast cancer could be considerably reduced by early-stage detection via appropriate screening examinations and procedures. Early detection would also ease the corresponding financial burden associated with late-stage breast cancer treatment, which was assessed to be around $2 billion in 2007 (2).

X-ray mammography represents the current gold standard for screening methodologies and is extensively used to detect breast cancer at an early stage (prominently in women who are asymptomatic), where treatment is more effective and a cure is more probable (3, 4). One of the primary features of diagnostic significance in mammograms is the presence of microcalcifications, which are tiny mineral deposits within the breast tissue and appear as small white spots on the X-ray film. Although there exists a close relationship between the nature of microcalcifications and disease type (5), mammograms do not provide sufficient information to reliably predict the tissue pathology (including normal tissue and benign and malignant lesions). Thus, as a follow-up procedure,

stereotactic breast biopsy is undertaken to remove tissue cores associated with the microcalcifications for examination by a pathologist under a microscope. Nevertheless, it is reported that microcalcifications are not successfully retrieved in almost 15% of stereotactic core needle biopsy procedures (6). In such cases, the absence of microcalcifications in the biopsied specimens leads to nondiagnostic or false negative biopsies, which places the patient at risk and potentially necessitates a repeat biopsy, often as a surgical procedure. There is, therefore, an unmet clinical need to develop a tool to detect microcalcifications in breast tissue that can provide real-time feedback to radiologists during stereotactic core needle biopsy procedures enabling more efficient retrieval of microcalcifications.

Optical spectroscopy provides a promising tool to address this unmet need and has been previously used by several research laboratories for tissue diagnosis (7–9). Structural changes are present in breast tissue that are used by pathologists to render traditional histopathology diagnoses, and spectroscopic analysis reveals changes in tissue composition that correlate with these changes in histopathology. Optical and spectroscopic modalities are more rigorous and objective than traditional pathologist interpretation as they provide a quantitative rather than qualitative assessment. In specific, diffuse reflectance, fluorescence, mid-infrared, and Raman spectroscopy have been extensively studied for discrimination of breast lesions (10–22) because of their ability to provide real-time diagnosis without necessitating the addition of exogenous contrast agents, which cannot be achieved with conventional histopathological examination. Furthermore, these modalities provide valuable biochemical information, which is lacking in mammographic diagnosis.

However, relatively less attention has been focused on the problem of microcalcification detection in such lesions. Given the application under consideration, in which there is an a priori expectation of abnormal tissue, accurate distinction of lesions with microcalcifications from those without microcalcifications is critical. Our group had originally distinguished between type I and II breast microcalcifications and discriminated type II microcalcifications associated with benign and malignant breast lesions in Raman microscopy studies of formalin-fixed, paraffin-

APPLIED BIOLOGICAL SCIENCES

embedded breast biopsies (23). We have recently extended this work to demonstrate the ability of Raman spectroscopy to identify microcalcifications in core needle breast biopsy specimens (24). Despite these promising results, a major drawback of Raman spectroscopy is its intrinsically weak signals (i.e., low sensitivity), which considerably amplifies the complexity of instrumentation (including optical fiber probes) and necessitates long acquisition times. This may substantially increase the overall biopsy procedure time, which is undesirable in terms of medical cost and patient convenience.

As alluded to previously, diffuse reflectance spectroscopy has been shown to provide comparable discrimination performance to Raman spectroscopy for breast cancer diagnosis (18). The diffuse reflectance measurements in the UV-visible region are typically used to quantify hemoglobin saturation, total hemoglobin concentration, beta-carotene concentration, and the mean reduced scattering coefficient, a combination of parameters that is subsequently used for tissue diagnosis. However, we suspected that the utility of reflectance information can also be extended to identify microcalcifications in the breast due to their unique structural and chemical features in relation to the neighboring tissue. Our hypothesis of reflectance-based microcalcification detection is supported by prior observations of changes in refractive index in breast tissue with microcalcifications (25) and laser-induced autofluorescence of similar calcified structures in atherosclerotic plaques (26). Because absorption and corresponding fluorescence emission spectra reflect transitions between identical vibronic states, we conjecture that, despite the relatively weak relationship with the underlying biochemistry, one can measure and use the latent information in diffuse reflectance spectra for accurate identification of microcalcification status.

In this article, we investigate the feasibility of using diffuse reflectance spectroscopy for identification of microcalcifications in freshly excised breast tissue. Our reflectance measurements reveal that the presence of microcalcifications in lesions manifests itself in subtle but consistent changes in spectral features, and the resultant decision algorithm shows excellent efficacy in classifying normal tissue as well as lesions with and without microcalcifications. A model of proteins (including elastin) and associated cross-linkers in the calcified clusters is proposed to explain the differential absorption signatures of the lesions with microcalcifications. It is surprising that the classification performance of the reflectance decision algorithm is comparable to that of the corresponding Raman algorithm. We envision that the substantive advantages of diffuse reflectance spectroscopy in terms of acquisition time and simpler instrumentation will enable its ready translation to clinical practice, optimizing the diagnostic value of the initial biopsy and thereby reducing the number of repeat biopsies currently required.

Results

Diffuse Reflectance Spectroscopy. Fig. 1 shows representative diffuse reflectance spectra acquired from normal human breast tissue (Fig. 1A), as well as those from tissue sites histopathologically designated as lesions without microcalcifications (Fig. 1B) and lesions with microcalcifications (Fig. 1C). Evidently, there are differences in the spectral signatures between the tissue sites of different classes, in particular between those acquired from normal sites and from sites with lesions. This is consistent with our laboratory's previous observations (18), where the normal tissue spectra were markedly different from those obtained from sites diagnosed as fibroadenoma, fibrocystic change, or cancer. The differences in the normal and lesion classes (such as the more pronounced absorption signal in the 450–490-nm region resulting in lower reflectance measurements in the normal tissue) can be primarily attributed to the presence of substantially higher β-carotene content in normal breast tissue. However, the differences between the lesion sites with microcalcifications and those without microcalcifications (i.e., between class) are more subtle. Further, small within-class variations in the spectral dataset impede the possibility of elucidating such differences by single-feature analysis.

Nevertheless, such changes can be detected using multivariate chemometric algorithms, as long as the between-class variations are consistent and exceed within-class spectral differences. Here, we have used principal component analysis (PCA) to reduce the dimensionality of the spectral dataset into key spectral components. Fig. 2 shows the first three principal components (PCs) of the diffuse reflectance spectral dataset in order of net variance explained by each. It is clear that PC1 and PC2 both highlight the oxy-hemoglobin absorption features, namely the Soret band at 414 nm and the Q bands at *ca.* 547 and 580 nm, with a shallow absorption trough at 563 nm. Also, PC3 shows a wider trough in the 430–490-nm region, which is well known to contain the β-carotene absorption features (typically at 450 and 480 nm, ref. 27) and, as such, is the primary determinant between normal tissue sites and those consisting of lesions. The successive PCs, as is expected, have more noise contributions. In this analysis, the selection of PCs in the support vector machine (SVM)-derived decision algorithm was governed by the net variance threshold (99.9%), as well as by the minimization of error in cross-validation. For our dataset, 10 PCs were found to be optimal for use in SVM decision algorithm building.

Previously, several investigators have analyzed the diffuse reflectance information in a different manner by incorporating mathematical models based on the diffusion approximation of light propagation in tissue to determine the reduced scattering coefficient $\mu_s'(\lambda)$ [and the A and B parameters, where $\mu_s'(\lambda) = A\lambda^{-B}$] and the concentration of the prevalent absorbers in the UV (UV)-visible region (hemoglobin and β-carotene) (7, 18, 28, 29). However, because we do not expect the contributions of these constituents to vary significantly among lesions with and without microcalcifications, we have chosen to use PCA to highlight the smaller variations that would be neglected by the light transport model and its variants.

To obtain a measure of its classification ability, we used the PC-based SVM decision algorithm in a leave-one-out cross-validation (LOOCV) analysis. Table 1 provides the confusion matrix for the SVM-derived model, where each column of the matrix represents
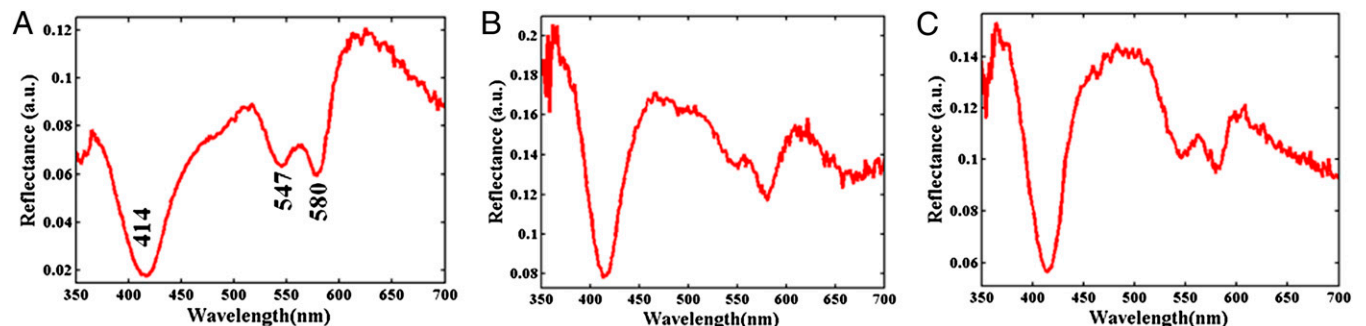
Fig. 1. Representative diffuse reflectance spectra acquired from breast tissue: (A) normal tissue site, (B) lesion without microcalcifications, and (C) lesion with microcalcifications.
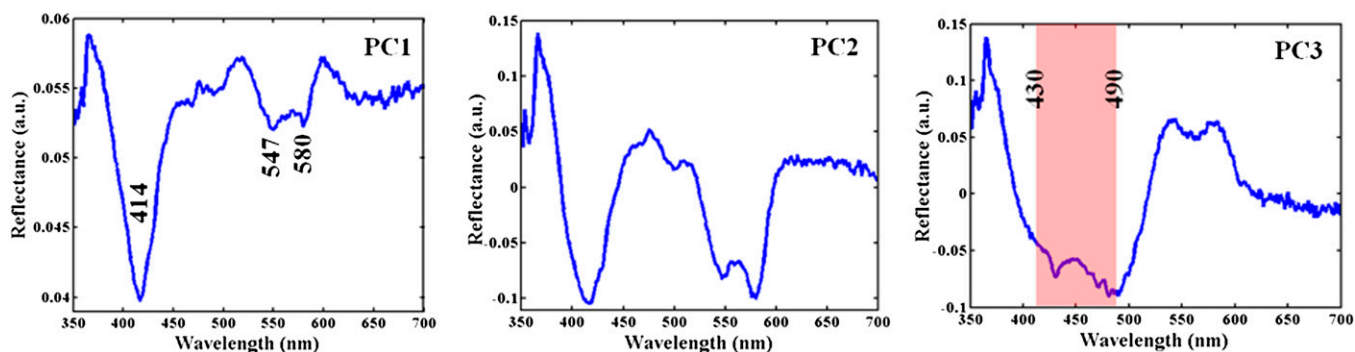
Fig. 2. Illustration of principal components for diffuse reflectance measurements. The first three principal components in order of net variance corresponding to the diffuse reflectance spectra acquired from the freshly excised breast tissue cores. PC1 and PC2 both demonstrate oxy-hemoglobin absorption features, namely the Soret band at 414 nm, and the Q bands at *ca.* 547 and 580 nm, with a shallow absorption trough at 563 nm. PC3 shows a wider trough in the 430–490-nm region, which contains β-carotene absorption features (typically at 450 and 480 nm).

the instances in a diffuse reflectance predicted class, and each row represents the instances in the reference (combined histopathologic and radiographic) class. In specific, for diagnosis of lesions with microcalcifications (which is the target class for our study), the decision algorithm provides a positive predictive value (PPV) of 97%, negative predictive value (NPV) of 88%, sensitivity (SE) of 67%, and specificity (SP) of 99%. The overall diagnostic accuracy (OA) for all classes was computed to be 77%. These results indicate that diffuse reflectance spectra provide high diagnostic power for detection of lesions with microcalcifications and can be suitably used as an adjunct to stereotactic core needle biopsy, particularly due to its excellent PPV.

In the clinical situation under consideration (i.e., the detection of microcalcifications in core needle biopsy procedures), PPV signifies the most important performance metric, because false positives could potentially have serious adverse consequences for the patient (30). This is representative of cases where the disease to be diagnosed is serious, should not be overlooked, and is treatable. Hence, it is imperative to confirm that biopsy tissue with a positive spectroscopic diagnosis of microcalcifications actually harbors microcalcifications as, in the case of a false positive, the radiologist may only retrieve a single core and miss the targeted lesion. As a further consequence, the patient may have to undergo a follow-up stereotactic or even a surgical biopsy. On the flip side, even if the spectroscopic algorithm indicates that the tissue to be biopsied does not harbor microcalcifications when it does (i.e., presents a false negative), the radiologist will remove (unnecessary) additional tissue cores. Although this is undesirable, it does not pose a major health risk to the patient.

In addition, to verify the robustness of our findings to potential spurious correlations in the spectral dataset, we implemented a negative control study (31). In particular, the three class labels (normal, lesion without microcalcifications, and lesion with microcalcifications) were assigned in a randomized order, irrespective of their true labels. Using the previously obtained PC scores along with the control labels, we derived an SVM decision algorithm, which gave PPV, NPV, and OA of 40%, 65%, and 44%, respectively. Even after multiple iterations, the PPV and OA of the

control models never exceeded 50%, highlighting the robustness of the proposed approach to confounding variables and chance correlations. This is notable because the reported experiments were performed over several weeks; one would expect that the algorithm(s) would not be subjected to systematic temporal correlations (including system drift) that may otherwise be expected in a single day or single sitting clinical study.

Fig. 3 exhibits the receiver operating characteristic (ROC) curve for diffuse reflectance diagnosis of lesions with microcalcifications. The ROC curve (in red) plots sensitivity versus (1-specificity) for the SVM decision algorithm as the discrimination threshold is varied. For comparison, the ROC curve of two indistinguishable classes (represented by the solid black line) is also shown in the figure. The area under the curve (AUC) is 0.88 in comparison with an AUC for a perfect algorithm of 1.00. It is pertinent to note that although a spectral algorithm to distinguish type I and II microcalcifications was not developed in the current study (because very few type I microcalcifications were present in the dataset), the proposed approach could potentially be extended to differentiate the types of microcalcifications.

Raman Spectroscopy. For the sake of comparison and completeness, the acquired Raman spectra from the tissue sites were subjected to the same analysis (PCA followed by SVM classification). The Raman spectra collected in this study were very similar to those acquired using an identical protocol for the Raman pilot study published in ref. 32. As was expected, the Raman spectra display features indicative of the presence of fat, collagen, calcium hydroxyapatite, and calcium oxalate. The latter two suggest the incidence of microcalcifications, with type I deposits consisting of calcium oxalate dehydrate and the type II deposits composed primarily of calcium hydroxyapatite (23). Fig. 4 shows the first three Raman principal components in order of net variance explained by each. Each of the PCs shows a number of Raman features along with increasing noise contributions in successive components. In particular, a number of the features of PC1 are consistent with those of fat and collagen, e.g., 1655 cm^{-1} amide-I band and 1447 cm^{-1} CH$_2$ deformation band. Here,

Table 1. Confusion matrix for LOOCV of SVM-derived diffuse reflectance-based decision algorithm

	SVM diffuse reflectance diagnosis		
Reference diagnosis	Normal	Lesion without microcalcifications	Lesion with microcalcifications
Normal	77	13	0
Lesion without microcalcifications	14	41	1
Lesion with microcalcifications	17	2	38

Each column of the matrix represents the instances in a spectroscopy predicted class, and each row represents the instances in the reference class.

Fig. 3. ROC curve for SVM-derived diffuse reflectance algorithm for the diagnosis of breast lesions with microcalcifications. The ROC curve in red plots sensitivity versus (1-specificity) for the SVM decision algorithm as the discrimination threshold is varied. For comparison, the ROC curve of two indistinguishable classes (represented by the solid black line) is also shown. The area under the curve is 0.88 compared with an AUC of 1.00 for a perfect algorithm (TP = true positive; FP = false positive).

too, the number of PCs retained in SVM decision algorithm building was decided by the minimization of error in LOOCV-based classification and was determined to be 10. Thus, for both the diffuse reflectance and Raman decision algorithms, the sample per feature ratio (SFR) is the same and in excess of 10, thereby enabling the development of a robust algorithm (33).

Table 2 provides the corresponding confusion matrix for the SVM-derived decision algorithm based on Raman measurements. In particular, we observe that the Raman decision algorithm provides a PPV of 98%, NPV of 95%, SE of 88%, and SP of 99% for diagnosis of lesions with microcalcifications. The overall accuracy for diagnosis of all classes was determined to be 81%. It is evident that although the biochemical specificity of Raman spectra (to the analytes of interest, such as calcium hydroxyapatite and oxalate) provides enhanced values for NPV (95%) and SE (88%) compared with those of the corresponding diffuse reflectance

decision algorithm (NPV = 88% and SE = 67%). It is also instructive to note that the SP and, more importantly, the PPV values of the two modalities are fairly comparable. A summary of the performance metrics for both the reflectance and Raman SVM decision algorithms is provided in Tables 1 and 2, respectively. Fig. 5 displays the ROC curve for the Raman SVM decision algorithm, which illustrates the ability of Raman spectroscopy to discriminate lesions with microcalcifications from normal breast tissue and lesions without microcalcifications. The area under the ROC curve (0.86) in Fig. 5 is found to be surprisingly comparable to the corresponding value for the reflectance decision algorithm (0.88).

Discussion

Our findings suggest that diffuse reflectance spectroscopy can be an important clinical tool for detection of breast lesions with microcalcifications. Therefore, it is important to consider the origin of the diffuse reflectance discriminatory capability. Diffuse reflectance spectroscopy is well characterized to provide two primary sources of information: elastic scattering and absorption (the interaction of which is often referred to as tissue turbidity in the biophotonics literature). The elastic scattering information is typically extracted in the form of a wavelength-dependent reduced scattering coefficient ($\mu_s'(\lambda)$), which itself is a function of the effective density of tissue scatterers (ρ_s) and effective reduced scattering cross-section ($\sigma'(\lambda,d_s)$), as noted in ref. 34. Although the effective density of tissue scatterers may vary due to the presence of microcalcification clusters, it is unlikely to have a significant impact on the more meaningful parameter of scattering cross-section $\sigma'(\lambda,d_s)$. This is because, although the individual microcalcifications have a median size of ~200 μm (with a range of *ca.* 20–1000 μm) (32), the slope of the scattering spectrum does not change significantly when the scatterer size is greater than 1.5 μm, as per Mie theory. Thus, we ascribe the source of the discrimination ability to the absorption component of the diffuse reflectance information.

The absorption component in the UV-visible region of interest has been previously modeled as consisting of two primary absorbers, namely hemoglobin (oxy and deoxy) and β-carotene. However, this represents a simplified mathematical model that does not account for smaller contributions of tissue absorbers, e.g., melanin, water, proteins, nucleic acids, and lipids (35). Indeed, we attribute the ability to diagnose microcalcifications using diffuse reflectance spectra to the presence of proteins (and related cross-linking molecules) associated with these calcified deposits. Our conjecture in this matter is supported by prior findings of laser-induced autofluorescence identification of calcified deposits in atherosclerotic human aorta (26, 36), which are similar in chemical composition to the microcalcifications found in breast tissue (23, 37). In particular, Baraga et al. (38) have shown that the autofluorescence spectra obtained from calcified deposits in human arterial walls have a similar lineshape to that obtained from elastin fibers. [It is

Fig. 4. Illustration of principal components for Raman measurements. The first three principal components corresponding to the Raman spectra from the freshly excised breast tissue cores. In particular, a number of the features of PC1 are consistent with those of fat and collagen, e.g., 1,655 cm⁻¹ amide-I band and 1,447 cm⁻¹ CH₂ deformation band.

Table 2. Confusion matrix for LOOCV of SVM-derived Raman spectroscopy-based decision algorithm

	SVM Raman diagnosis		
Reference diagnosis	Normal	Lesion without microcalcifications	Lesion with microcalcifications
Normal	73	16	1
Lesion without microcalcifications	15	41	0
Lesion with microcalcifications	7	0	50

well known that the mineral component of calcified deposits does not fluoresce in the wavelength region under consideration (26).] This interpretation is further bolstered by the supporting evidence of Movat-stained sections of calcified plaque, in which regions of the calcified deposit had the staining characteristics of elastin.

Moreover, because the electronic transition (in absorption and fluorescence emission) does not greatly alter the nuclear geometry in the molecule, the fluorescence emission spectrum exhibits a one-to-one correspondence with the absorption spectrum of the ground–to–first-excited-state transition. This constitutes the mirror image rule and implies that the vibration structures seen in absorption and emission spectra are similar (39). Although there are some exceptions to the strict interpretation of this rule, there is always a direct correlation between the absorption process and the subsequent emission for any fluorophore. Based on this understanding, as well as the aforementioned fluorescence microscopy studies of calcified deposits, one can reasonably infer that the proteins (such as elastin) linked with the microcalcifications have a contribution to the absorption component of the diffuse reflectance spectra. Also, based on the fluorescence observations, we may estimate that the absorption contribution of such features in our reflectance spectra is present in the UV and lower wavelength ranges of the visible region. The proposed model is also consistent with prior reports of elastin, and associated cross-linkers such as desmosine and isodesmosine, displaying a broad range of absorption spectra from below 300 nm to above 400 nm (40).

Conclusions

In the present study, we have proposed and demonstrated the potential of diffuse reflectance spectroscopy for detection of microcalcifications in freshly excised tissue from patients undergoing breast core needle biopsies. It is observed that the reflectance information shows high efficacy in tissue pathology classification and, importantly, provides a positive predictive value of 97% for the diagnosis of lesions with microcalcifications, which form the target class of any core needle biopsy procedure. We also note that the decision algorithm is robust to the incidence of spurious correlations and that the underlying characterization capability of the algorithm can be attributed to the presence of elastin and desmosine and isodesmosine cross-links in the microcalcifications. The performance metrics of the reflectance modality are surprisingly similar to that of Raman spectroscopy, albeit with a significantly shorter acquisition time. Given our findings and the inherent attributes of diffuse reflectance spectroscopy, this approach would appear to be particularly appropriate as a real-time clinical adjunct to stereotactic core needle biopsy. The proposed approach lends itself to facile assembly of a side-viewing probe that could be inserted into the central channel of the biopsy needle for intermittent acquisition of the reflectance spectra, which would, in turn, reveal whether or not the tissue to be biopsied contains the targeted microcalcifications. A dedicated diffuse reflectance probe would be simpler in design and could be smaller in outer diameter than a dedicated Raman probe or the unitary multimodality probe used in this study, enabling diffuse reflectance measurements during a wider range of breast biopsy procedures, such as ultrasound-guided needle biopsy, that use narrower gauge biopsy needles than those typically used for stereotactic breast biopsy. In the near future, this could considerably improve the accuracy of the diagnostic efforts, thereby reducing the necessity for repeat biopsies, without requiring development and assembly of complex and costly optical systems. In addition, although the cross-validation studies performed here provide the foundation for diagnosis of breast lesions with microcalcifications using diffuse reflectance spectroscopy, further clinical investigations will be pursued to validate the proposed approach prospectively using completely independent samples. The performance of the SVM-derived algorithm may decrease (slightly) when tested in large-scale studies in more diverse patient populations. Depending on the variety of breast lesions and the complexity of tissue biochemical composition encountered in these studies, implementation of alternate chemometric classification methods may also be explored.

Materials and Methods

Patient Population and Tissue Preparation. The ex vivo clinical study was carried out at University Hospitals-Case Medical Center (UH-CMC) Breast Center, Cleveland, OH. The study was approved by the UH-CMC Institutional Review Board and the Massachusetts Institute of Technology Committee on the Use of Humans as Experimental Subjects. Informed consent for the reported experiments was obtained from all subjects before their biopsy procedures.

Measurements were acquired from female patients (age range of 39–78 y) undergoing stereotactic breast needle biopsies for microcalcifications detected at screening mammography. Data were collected ex vivo from fresh breast needle biopsy tissue cores within 30 min of excision. Overall, 203 sites on biopsy tissue cores removed from 23 patients were analyzed. The tissue cores were
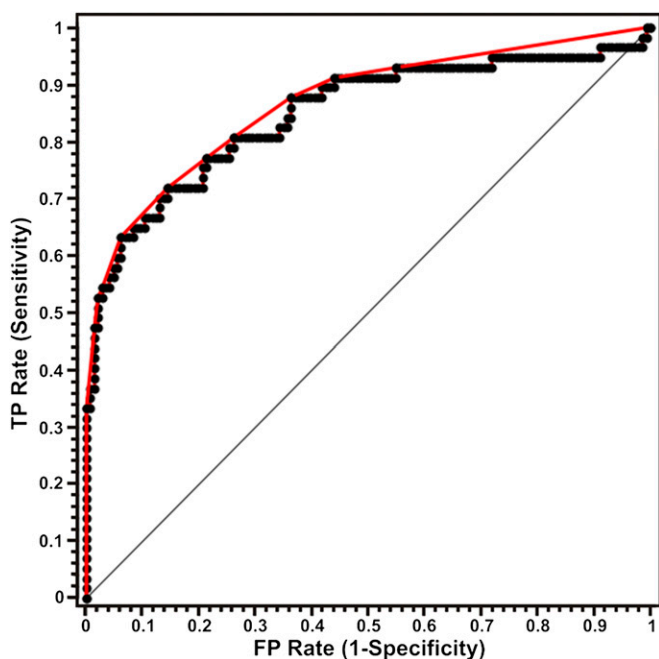
Fig. 5. ROC curve for support vector machine-derived Raman algorithm for the diagnosis of breast lesions with microcalcifications. The ROC curve in red plots sensitivity versus (1-specificity) for the SVM decision algorithm as the discrimination threshold is varied. The ROC curve of two indistinguishable classes is represented by the solid black line. The area under the curve is 0.86, which is lower than that for the diffuse reflectance algorithm (0.88) (TP = true positive; FP = false positive).

~2.0 cm in length and ranged from 1.0 to 2.8 mm in maximum diameter, determined by the geometry of the 9-gauge biopsy needle.

After acquisition of diffuse reflectance and Raman spectra (as detailed in the following paragraphs), the specimen sites were marked with colloidal inks, fixed in 10% (vol/vol) neutral buffered formalin and paraffin embedded. Tissue sections were subsequently obtained and hematoxylin/eosin stained for microscopic examination by a breast pathologist, who was blinded to the spectroscopic evaluation. The radiographic assessments based on the specimen radiograph and the histopathology diagnoses were used in conjunction to provide the final gold standard for comparison with spectroscopic results.

The combined radiography and histopathology assessment was used to classify the 203 breast tissue sites into three classes: 90 normal sites, 56 lesions without microcalcifications, and 57 lesions with microcalcifications. The histopathology diagnoses for the 203 breast tissue sites were as follows: 91 normal tissues, 98 fibrocystic change, 2 fibroadenoma, 4 ductal carcinoma in situ, and 8 invasive ductal carcinoma. One of the normal sites revealed microcalcification clusters on radiographic assessment and was therefore reassigned to the lesion with microcalcifications category.

Instrumentation. Diffuse reflectance and Raman spectroscopic measurements were performed using a portable, compact clinical system (instrument and optical fiber probe), described in detail in ref. 41. In brief, this instrument contains: a xenon flash lamp (370–740 nm) to obtain diffuse reflectance spectra, and a diode laser (830 nm) for Raman excitation. The instrument employs a unitary optical fiber probe that allows sequential collection of reflectance and Raman spectra from the same tissue site. The probe contains a single excitation fiber and a concentric ring of 15 collection fibers, 10 of which are used to collect Raman spectra, and the remaining 5 collect diffuse reflectance spectra. The average laser excitation power delivered to the tissue was ~100 mW over a 1 mm^2 spot, while the Xe lamp provided a 2.9-μs

full width at half maximum (FWHM) white light pulse, 1 J/pulse maximum. The acquisition time for the two modalities combined was 5.6 s for 10 frames (Raman acquisition time per frame was 500 ms; diffuse reflectance acquisition time per frame was 60 ms). The fluences used in the experiments are safe for clinical investigations and no tissue damage was observed on histological examination.

For spectral acquisition, the probe was gently brought into contact with the tissue specimen and the spectra were collected with room lights off as the Raman signal is weak in relation to the ambient background light. Spectra were recorded from multiple tissue sites of interest from each tissue core as well as from several cores in each biopsy, and thus the number of collected spectra varied from patient to patient. The collected spectra were dispersed via two spectrographs and recorded using two CCD detectors, one optimized for near-infrared detection (Raman) and the other for UV-visible wavelengths (diffuse reflectance).

Spectral Data Analysis. The reflectance spectra were wavelength calibrated using a mercury spectrum and were subjected to dark noise and flat field correction before further analysis. Similarly, the Raman shift axis was calibrated using a 4-acetaminophen spectrum and the acquired spectra were further corrected for the probe background and the spectrograph-detector response (24). Following the preprocessing steps, the reflectance and Raman spectra were subjected to PCA for dimensional reduction and subsequently to SVM analysis for classifier model development. Further details of the data analysis are provided in the *SI Text*.

1. American Cancer Society (2012) *Cancer Facts & Figures 2012* (Am Cancer Soc, Atlanta).
2. Centers for Disease Control and Prevention. Screening to prevent cancer deaths. Available at www.cdc.gov/NCCdphp/publications/factsheets/Prevention/cancer.htm.
3. Rim A, Chellman-Jeffers M, Fanning A (2008) Trends in breast cancer screening and diagnosis. *Cleve Clin J Med* 75(Suppl 1):S2–S9.
4. Eddaoudi F, Regragui F (2011) Microcalcifications detection in mammography images using texture coding. *Appl Math Sci* 5(8):381–393.
5. Radi MJ (1989) Calcium oxalate crystals in breast biopsies. An overlooked form of microcalcification associated with benign breast disease. *Arch Pathol Lab Med* 113(12):1367–1369.
6. Jackman RJ, Rodriguez-Soto J (2006) Breast microcalcifications: Retrieval failure at prone stereotactic core and vacuum breast biopsy—Frequency, causes, and outcome. *Radiology* 239(1):61–70.
7. Richards-Kortum R, Sevick-Muraca E (1996) Quantitative optical spectroscopy for tissue diagnosis. *Annu Rev Phys Chem* 47:555–606.
8. Shah N, et al. (2001) Noninvasive functional optical spectroscopy of human breast tissue. *Proc Natl Acad Sci USA* 98(8):4420–4425.
9. Frangioni JV (2008) New technologies for human cancer imaging. *J Clin Oncol* 26(24):4012–4021.
10. Peters VG, Wyman DR, Patterson MS, Frank GL (1990) Optical properties of normal and diseased human breast tissues in the visible and near infrared. *Phys Med Biol* 35(9):1317–1334.
11. Breslin TM, et al. (2004) Autofluorescence and diffuse reflectance properties of malignant and benign breast tissues. *Ann Surg Oncol* 11(1):65–70.
12. Haka AS, et al. (2005) Diagnosing breast cancer by using Raman spectroscopy. *Proc Natl Acad Sci USA* 102(35):12371–12376.
13. Tromberg BJ, et al. (2005) Imaging in breast cancer: Diffuse optics in breast cancer: detecting tumors in pre-menopausal women and monitoring neoadjuvant chemotherapy. *Breast Cancer Res* 7(6):279–285.
14. Haka AS, et al. (2006) *In vivo* margin assessment during partial mastectomy breast surgery using Raman spectroscopy. *Cancer Res* 66(6):3317–3322.
15. Corlu A, et al. (2007) Three-dimensional in vivo fluorescence diffuse optical tomography of breast cancer in humans. *Opt Express* 15(11):6696–6716.
16. Stone N, Baker R, Rogers K, Parker AW, Matousek P (2007) Subsurface probing of calcifications with spatially offset Raman spectroscopy (SORS): Future possibilities for the diagnosis of breast cancer. *Analyst (London)* 132(9):899–905.
17. Majumder SK, Keller MD, Boulos FI, Kelley MC, Mahadevan-Jansen A (2008) Comparison of autofluorescence, diffuse reflectance, and Raman spectroscopy for breast tissue discrimination. *J Biomed Opt* 13(5):054009.
18. Volynskaya Z, et al. (2008) Diagnosing breast cancer using diffuse reflectance spectroscopy and intrinsic fluorescence spectroscopy. *J Biomed Opt* 13(2):024012.
19. Stone N, Matousek P (2008) Advanced transmission Raman spectroscopy: A promising tool for breast disease diagnosis. *Cancer Res* 68(11):4424–4430.
20. Brown JQ, et al. (2009) Quantitative optical spectroscopy: A robust tool for direct measurement of breast cancer vascular oxygenation and total hemoglobin content in vivo. *Cancer Res* 69(7):2919–2926.
21. Haka AS, et al. (2009) Diagnosing breast cancer using Raman spectroscopy: Prospective analysis. *J Biomed Opt* 14(5):054023.
22. Bhargava R (2012) Infrared spectroscopic imaging: The next generation. *Appl Spectrosc* 66(10):1091–1120.
23. Haka AS, et al. (2002) Identifying microcalcifications in benign and malignant breast lesions by probing differences in their chemical composition using Raman spectroscopy. *Cancer Res* 62(18):5375–5380.
24. Saha A, et al. (2011) Raman spectroscopy: A real-time tool for identifying microcalcifications during stereotactic breast core needle biopsies. *Biomed Opt Express* 2(10):2792–2803.
25. Wang Z, Tangella K, Balla A, Popescu G (2011) Tissue refractive index as marker of disease. *J Biomed Opt* 16(11):116017.
26. Verbunt RJAM, et al. (1992) Characterization of ultraviolet laser-induced autofluorescence of ceroid deposits and other structures in atherosclerotic plaques as a potential diagnostic for laser angiosurgery. *Am Heart J* 123(1):208–216.
27. Angheloiu GO, et al. (2006) Intrinsic fluorescence and diffuse reflectance spectroscopy identify superficial foam cells in coronary plaques prone to erosion. *Arterioscler Thromb Vasc Biol* 26(7):1594–1600.
28. Farrell TJ, Patterson MS, Wilson B (1992) A diffusion theory model of spatially resolved, steady-state diffuse reflectance for the noninvasive determination of tissue optical properties *in vivo*. *Med Phys* 19(4):879–888.
29. Georgakoudi I, et al. (2001) Fluorescence, reflectance, and light-scattering spectroscopy for evaluating dysplasia in patients with Barrett's esophagus. *Gastroenterology* 120(7):1620–1629.
30. Fitzmaurice M (2000) Principles and pitfalls of diagnostic test development: Implications for spectroscopic tissue diagnosis. *J Biomed Opt* 5(2):119–130.
31. Barman I, et al. (2012) Raman spectroscopy-based sensitive and specific detection of glycated hemoglobin. *Anal Chem* 84(5):2474–2482.
32. Saha A, et al. (2012) Precision of Raman spectroscopy measurements in detection of microcalcifications in breast needle biopsies. *Anal Chem* 84(15):6715–6722.
33. Somorjai RL, Dolenko B, Baumgartner R (2003) Class prediction and discovery using gene microarray and proteomics mass spectroscopy data: Curses, caveats, cautions. *Bioinformatics* 19(12):1484–1491.
34. Zonios G, et al. (1999) Diffuse reflectance spectroscopy of human adenomatous colon polyps in vivo. *Appl Opt* 38(31):6628–6637.
35. Brown DL (2002) *Cardiovascular Plaque Rupture* (CRC Press, New York).
36. Fitzmaurice M, et al. (1989) Argon ion laser-excited autofluorescence in normal and atherosclerotic aorta and coronary arteries: Morphologic studies. *Am Heart J* 118(5 Pt 1):1028–1038.
37. Buschman HP, et al. (2001) Raman microspectroscopy of human coronary atherosclerosis: Biochemical assessment of cellular and extracellular morphologic structures *in situ*. *Cardiovasc Pathol* 10(2):69–82.
38. Baraga JJ, et al. (1990) Laser induced fluorescence spectroscopy of normal and atherosclerotic human aorta using 306-310 nm excitation. *Lasers Surg Med* 10(3):245–261.
39. Lakowicz JR (1999) *Principles of Fluorescence Spectroscopy* (Springer, New York).
40. Jones JDC, Webb CE (2003) *Handbook of Laser Technology and Applications* (Taylor & Francis, Oxford, UK).
41. Ŝćepanović OR, et al. (2009) A multimodal spectroscopy system for real-time disease diagnosis. *Rev Sci Instrum* 80(4):043103.